NANO LETTERS

pubs.acs.org/NanoLett Letter

Metal–Polyphenol Network Confined Synthesis of Nanozymes with Programmable Oxygen Vacancies for UVB Photodamage Therapy

Xiaomiao Cui, Jiawen Han, Tong Li, Wanling Liu, Qi Sun, Fuying Zhu, Congzhong Yang, Daoqing Fan, and Hui Wei*

Cite This: https://doi.org/10.1021/acs.nanolett.6c01558 Read Online

ACCESS | Metrics & More | Article Recommendations | Supporting Information

ABSTRACT: Conventional sunscreens block ultraviolet B (UVB) but fail to scavenge accumulated reactive oxygen species (ROS), causing severe photodamage. Herein, we develop a room-temperature, aqueous coordination strategy that assembles metal–polyphenol networks (MPNs) to confine *in situ* nucleation and growth of metal oxide nanozymes. Utilizing tannic acid coordinated ceria (CeO_2-TA) as a model system, we achieve programmable regulation of surface oxygen vacancies (O_v) by adjusting the ligand-to-metal molar ratio. This process involves ligand-to-metal charge transfer (LMCT) mediated interfacial electron redistribution, resulting in significant enhancements in superoxide dismutase (SOD)- and catalase (CAT)-like activities. This "ligand-unit equivalence" design is universally applicable across diverse polyphenols, yielding highly dispersed and catalytically efficient nanozymes. *In vivo*, topical CeO_2-TA profoundly scavenges UVB-induced ROS, mitigating acute skin inflammation and preserving the extracellular matrix against photoaging. This work establishes a universal and scalable method for the development of O_v engineered nanozymes and promotes their integration into next-generation topical sunscreens.

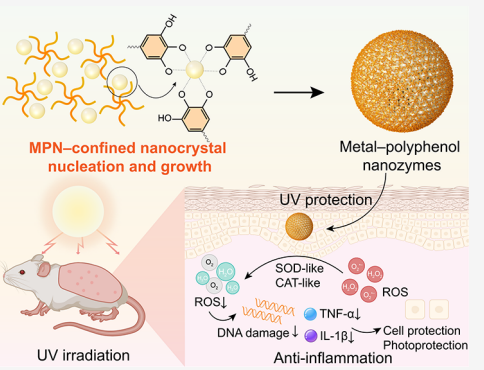

KEYWORDS: *nanozymes, metal–polyphenol network, oxygen vacancies, antioxidant activity, photodamage therapy*

Prolonged solar ultraviolet B (UVB) exposure drives excessive reactive oxygen species (ROS) production, causing oxidative damage to cellular lipids, proteins, and genomic DNA and triggering severe skin inflammation and photoaging.[1−5] When antioxidant defenses are overwhelmed, excessive oxidative stress induces cell apoptosis or necrosis. Meanwhile, sublethal oxidative stress activates various inflammation-related signaling pathways, thereby exacerbating skin inflammation.[2,6,7] Conventional sunscreens primarily rely on UVB absorbers or scatterers.[3,8] They decrease incident UVB but do not address downstream oxidative and inflammatory effects.[9] Furthermore, uncertainties concerning long-term biocompatibility,[10] the limited duration of ROS scavenging capacity, and the inadequate modulation of immune and inflammatory pathways constrain their capacity to deliver comprehensive and enduring photoprotection during ongoing UVB exposure.[11]

Benefiting from tunable properties and robust enzyme-mimetic activities, nanozymes have emerged as highly versatile catalytic platforms.[12−15] Antioxidant nanozymes can regulate ROS levels by mimicking enzymes such as superoxide dismutase (SOD) and catalase (CAT), demonstrating potential applications in biomedical engineering.[16−20] Among these, metal oxide nanozymes such as cerium dioxide (CeO_2) are particularly attractive for interventions related to inflammation,[21,22] especially in the skin,[23] owing to their reversible Ce^{3+}/Ce^{4+} redox cycling and generally advantageous biocompatibility.[24−27] Critically, the enzyme-like activity of metal oxide nanozymes is profoundly influenced by surface defect states, particularly the density and accessibility of oxygen vacancies.[28−30] Therefore, precisely engineering the oxygen vacancy density is essential. However, establishing a high density of oxygen vacancies while preserving the colloidal stability to maintain the accessibility of vacancy-associated active sites remains a challenge. Several approaches have been explored to enrich oxygen vacancy populations, including chemical reduction,[31] aliovalent ion doping,[28] thermal annealing,[32] pressure,[33] and high-energy irradiation,[34,35] typically relying on harsh thermal or reducing conditions. These treatments further exacerbate the intrinsic thermodynamic instability of high-surface-energy nanocrystals, driving irreversible aggregation.[36,37] Such irreversible agglomeration reduces the accessibility of oxygen vacancy-associated active sites, imposes mass-transport limitations, and hinders interfacial electron/proton transfer, thereby diminishing the

Received: April 1, 2026
Revised: June 1, 2026
Accepted: June 2, 2026

https://doi.org/10.1021/acs.nanolett.6c01558
Nano Lett. XXXX, XXX, XXX−XXX

Scheme 1. MPN-Confined Synthesis of Metal−Polyphenol Nanozymes with Programmable Oxygen Vacancies for UVB-Induced Skin Photodamage Therapy: (a) Programmable Regulation of Oxygen Vacancies and Enzyme-like Activities *via* Tuning the Polyphenol-to-Metal Ratio during Confined Nucleation; (b) Topical Application of Nanozymes to Scavenge ROS, Attenuate Inflammation, and Promote Photodamage Repair.

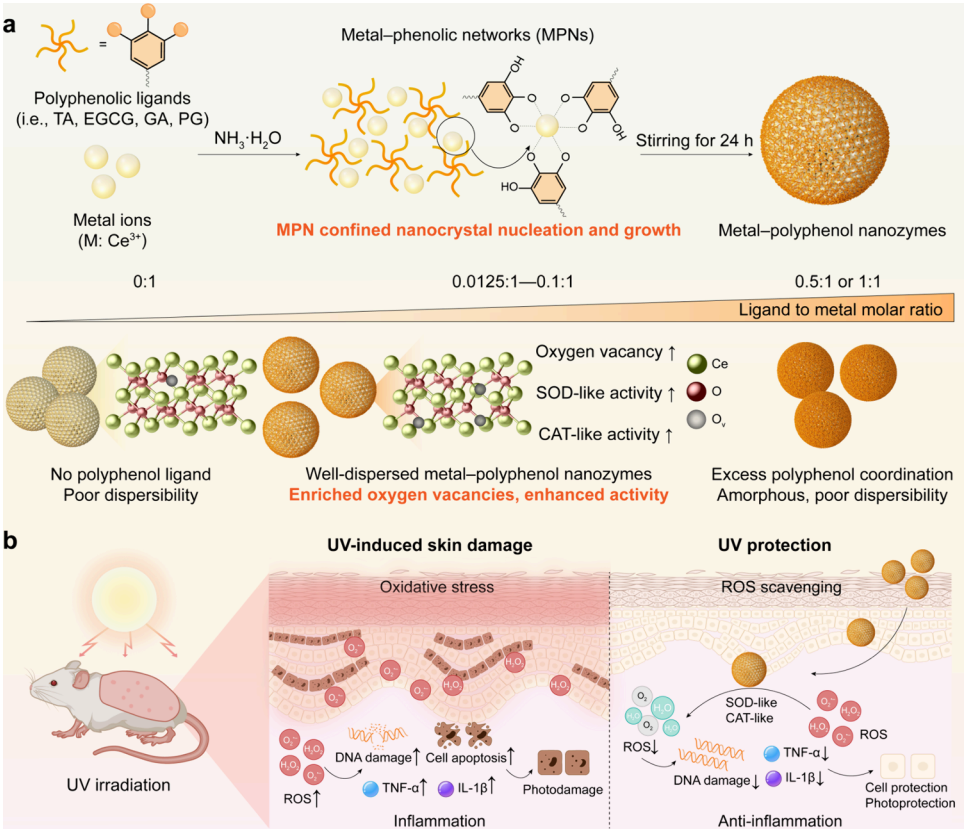

catalytic efficiency of nanozymes. Additionally, it may adversely affect dispersibility and stability in practical applications.[25,38] Polymer or small-molecule ligands remain the primary approach for enhancing nanocatalyst stability and dispersibility. However, such ligands often exhibit biological inertness, limiting precise regulation of surface electronic structures and interfacial microenvironments,[39−41] thereby restricting their capacity to modulate enzyme-like activity. Therefore, a generalizable and mild strategy that concurrently suppresses agglomeration and enables precise oxygen vacancy engineering is urgently needed.

Herein, we utilize the versatile coordination between small-molecule polyphenols and metal ions,[42−47] to construct metal−polyphenol networks (MPNs) with programmable physicochemical and biological functionalities.[48] This network assembles *in situ* to confine the nucleation and growth of metal oxide nanozymes, thereby generating highly dispersed, colloidally stable nanocrystals with maintained active site accessibility and efficient mass transport. Furthermore, ligand to metal charge transfer (LMCT)[49] and the mild electron-donating nature of polyphenols induce and stabilize surface oxygen vacancies, enabling controllable oxygen vacancy density (Scheme 1a). The intrinsic antioxidant properties of polyphenols combined with oxygen vacancy engineering significantly enhance the enzyme-like catalytic activity of antioxidant nanozymes. Consequently, this strategy presents a promising approach for the effective and sustainable regulation of ROS, as well as the treatment and prevention of UVB-induced skin inflammation (Scheme 1b).

PREPARATION AND CHARACTERIZATION OF METAL−POLYPHENOL NANOZYMES

Tannic acid (TA) contains numerous phenolic hydroxyl groups (−OH), exhibiting multidentate coordination properties.[44,50] Under mildly alkaline conditions, deprotonated TA coordinates metal ions (e.g., Ce^{3+}) to self-assemble into an MPN. Concurrently, TA confers mild electron-donating capability and intrinsic antioxidant capacity, while the induced LMCT effectively modulates the interfacial electronic structure. Based on these properties, TA is an effective ligand and building block for achieving confinement-assisted nanocrystal dispersion and tunable surface oxygen vacancies (O_v). Therefore, to investigate the influence of MPNs on nanocrystal dispersion and O_v engineering in CeO_2, we established an aqueous, room-temperature, *in situ* confinement-assisted synthesis method to prepare TA-coordinated cerium oxide nanozymes (CeO_2-TA).

Specifically, $Ce(NO_3)_3{\cdot}6H_2O$ was combined with TA in an aqueous solution. Upon adjusting the pH to a slightly alkaline level with dilute ammonia, a TA−Ce network formed rapidly. This network sequestered the cerium precursors and imposed nanoscale confinement on subsequent nucleation and crystal growth. Under these MPN-confinement conditions, slow oxidative crystallization at room temperature resulted in uniformly dispersed CeO_2-TA nanocrystals. Bare CeO_2 prepared in the absence of polyphenolic ligands served as the control (Figure 1a, b). Furthermore, a ligand equivalence gradient (TA:Ce = 0, 0.0125, 0.025, 0.05, 0.1, 0.5, and 1) was

https://doi.org/10.1021/acs.nanolett.6c01558
Nano Lett. XXXX, XXX, XXX−XXX

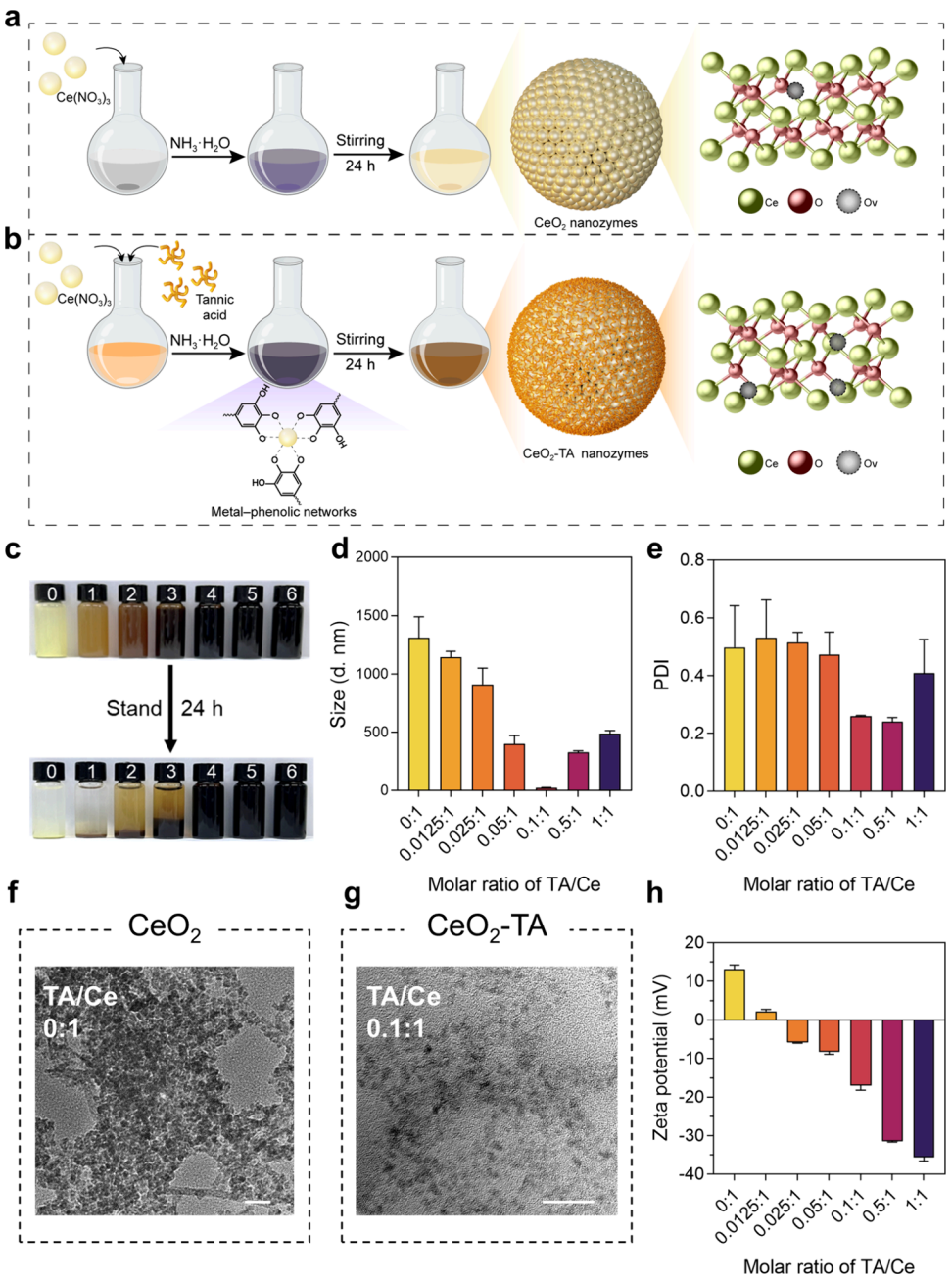

Figure 1. Preparation and characterizations of metal−polyphenol nanozymes. Schematic diagram of the preparation process of bare CeO_2 (without polyphenol ligands) (a) and CeO_2-TA nanozymes (b). (c) Photographs of metal−polyphenol nanozymes prepared with increasing ligand content. From left to right (0−6), the TA:Ce molar ratios are 0, 0.0125, 0.025, 0.05, 0.1, 0.5, and 1. Hydrodynamic diameter (d) and polydispersity index (e) of metal−polyphenol nanozymes. TEM images of CeO_2 (f) and CeO_2-TA (g). Scale bars: 10 nm. (h) Zeta potential of metal−polyphenol nanozymes. Data are presented as mean ± SD (n = 3).

used to systematically assess the influence of polyphenols on the synthesis of nanozymes. As shown in Figure 1c, after 24 h of quiescent storage, a TA-free (bare) CeO_2 dispersion exhibited pronounced sedimentation. In addition, dynamic light scattering (DLS) analysis showed that both the hydrodynamic diameter (Figure 1d) and polydispersity index (PDI) (Figure 1e) of the CeO_2-TA nanozymes initially decreased and then increased as the molar amount (polyphenol/Ce ratio) of the polyphenol ligand was raised. When the polyphenol ligand equivalence was 0.1, the hydrodynamic diameter reached a minimum size (~24.7 nm), indicating optimal dispersion under these conditions. Transmission electron microscopy (TEM) imaging further confirmed that uncoated CeO_2 nanoparticles exhibited significant aggregation and morphological heterogeneity (Figure 1f). At a ligand equivalence of TA:Ce = 0.1, the particles were uniformly dispersed (Figure 1g), with an average crystal size of ~3.5 nm (Figure S1). These observations indicated that the MPN effectively confines nucleation and growth, yielding uniformly small and highly dispersed nanocrystals, which proved advantageous for transdermal therapy of skin inflammation. Additionally, the zeta potential of the metal−polyphenol nanozymes became more negative as

https://doi.org/10.1021/acs.nanolett.6c01558
Nano Lett. XXXX, XXX, XXX−XXX

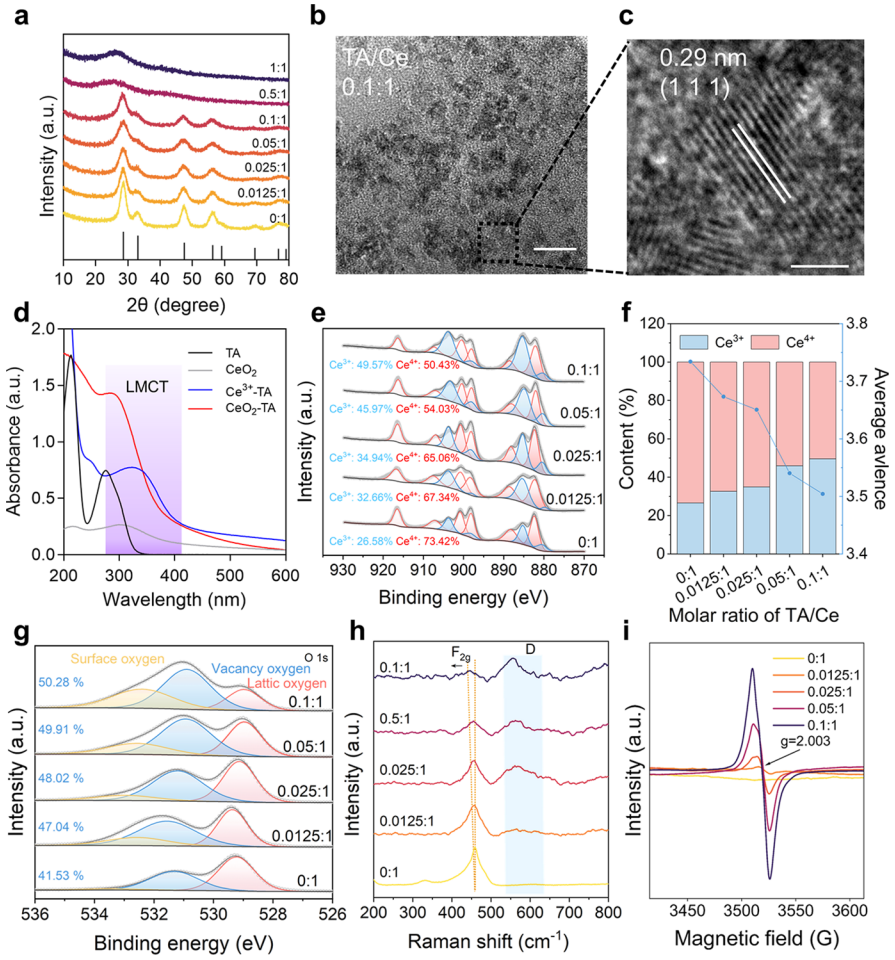

Figure 2. Ligand-programmed oxygen vacancy engineering in metal−polyphenol nanozymes. (a) XRD diffraction patterns of metal−polyphenol nanozymes. (b) High-resolution TEM image of CeO_2-TA and (c) lattice fringes of a CeO_2 nanocrystal. Scale bars: 10 and 2 nm, respectively. (d) UV−vis absorption spectra of TA, CeO_2, Ce^{3+}-TA, and CeO_2-TA (the TA:Ce molar ratios are 0.1). (e) Ce 3d XPS spectra of metal−polyphenol nanozymes. (f) Relative concentration of Ce^{3+} and average Ce valence state in the metal−polyphenol nanozymes. (g) O 1s XPS spectra of metal−polyphenol nanozymes. (h) Raman spectra of the metal−polyphenol nanozymes. (i) EPR spectra of the metal−polyphenol nanozymes.

ligand equivalence increased (Figure 1h), indicating successful modification of the phenol ligand.

To evaluate the effect of MPN confinement on crystal structure, X-ray diffraction (XRD) patterns of the metal−polyphenol nanozymes were measured. When the polyphenol ligand equivalent was less than or equal to 0.1 (five samples), all patterns showed the characteristic diffraction signals of cubic fluorite-type CeO_2 (PDF 00-034-0394) with no additional impurity peaks. Furthermore, the diffraction peaks of CeO_2-TA exhibited modest peak broadening that increased with ligand equivalence (Figure 2a), consistent with a reduction in coherent crystallite size. High-resolution TEM (HRTEM) images showed lattice fringes assignable to the CeO_2 (111) planes (Figure 2b, c), corroborating the phase identified by XRD, and further demonstrated a contracted $d_{(111)}$ spacing of ∼0.29 nm relative to the standard ∼0.31 nm of CeO_2, indicating confinement-induced lattice strain caused by polyphenol coordination and the restricted growth environment established by the MPN framework. However, at higher ligand equivalents (TA:Ce = 0.5 or 1.0), the characteristic diffraction peaks of CeO_2 disappeared, and the diffraction pattern was mainly composed of a broad amorphous peak, which was attributable to the organic MPN/carbonaceous matrix. This could be due to the excessive coordination of polyphenols, which hindered the oxidative growth of crystals. In the Fourier transform infrared (FTIR) spectra of CeO_2-TA (TA:Ce = 0.1), bands assignable to the galloyl/ester carbonyl (ν(C═O), ∼1719 cm^{-1}) and aromatic ring stretching (Ar ν(C═C), ∼1607 cm^{-1}) were attenuated and shifted, while the vibrations of δ(C−H) at ∼1444 cm^{-1}, ν(C−O) at ∼1317 cm^{-1}, and aromatic ν(C═C) at ∼1531 cm^{-1} exhibited discernible shifts and splitting, supporting the coordination interaction between the Ce ion and the −OH group of the polyphenol ligand (Figure S2). Furthermore, a broad absorption band in the UV−vis spectrum at 300−400 nm, which was attributed to LMCT from phenolate donors to Ce centers, corroborated polyphenol coordination and MPN formation (Figure 2d). Furthermore, to assess whether MPN confinement enabled controlled engineering of surface O_v, X-ray photoelectron spectroscopy (XPS) was performed on the Ce 3d and O 1s regions (excluding samples with polyphenol ligand equivalents of TA:Ce = 0.5 and 1.0, contained within an amorphous MPN matrix). Figure S3 presented the survey XPS spectrum of the metal−polyphenol nanozymes, confirming the presence of Ce, O, and C. Deconvolution of the multicomponent Ce 3d envelope showed that the Ce^{3+} fraction increased from 26.58% to 49.57% with increasing ligand equivalence, accompanied by the decrease in average Ce

https://doi.org/10.1021/acs.nanolett.6c01558
Nano Lett. XXXX, XXX, XXX−XXX

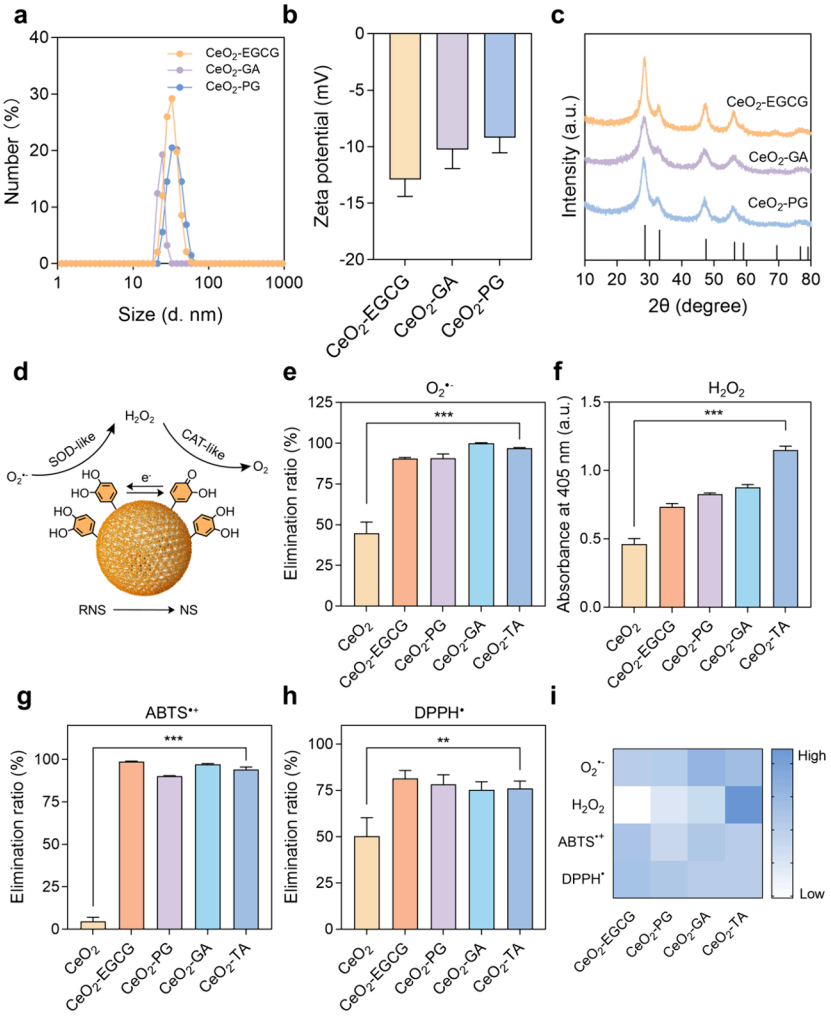

Figure 3. Versatile synthesis and antioxidant activity of metal−polyphenol nanozymes. Hydrodynamic diameter (a) and zeta potential (b) of CeO_2-EGCG, CeO_2-GA, and CeO_2-PG. Data are presented as mean ± SD (n = 3). (c) XRD diffraction patterns of CeO_2-EGCG, CeO_2-GA, and CeO_2-PG. (d) Schematic illustration of the ROS and reactive nitrogen species (RNS) scavenging capacities of metal−polyphenol nanozymes. SOD-like (e) and CAT-like (f) activities of metal−polyphenol nanozymes. $ABTS^{\bullet+}$ (g) and $DPPH^{\bullet}$ (h) radical scavenging capacity of metal−polyphenol nanozymes. Data are presented as mean ± SD (n = 3). (i) Heat map summarizing the antioxidant performance of metal−polyphenol nanozymes.

valence (Figure 2e, f). The O 1s spectra were separated into three peaks: lattice oxygen (O_{latt}), vacancy-related oxygen (O_v), and adsorbed oxygen (O_{ads}). The O_v proportion increased from 41.53% in bare CeO_2 to 50.28% in CeO_2-TA (Figure 2g). These trends indicated that MPN confinement of CeO_2-TA nanozymes enriched the surface oxygen vacancies.

Furthermore, Raman spectroscopy was performed to evaluate the tunability of defects in metal−polyphenol nanozyme structures. As shown in Figure 2h, the ∼456 cm^{-1} band corresponded to the triply degenerate F_{2g} mode of CeO_2 (Ce−O symmetric stretching), while the defect-induced band (D) at 550−610 cm^{-1} was associated with surface/near-surface disorder and oxygen vacancies. Relative to bare CeO_2, increasing ligand equivalence led to a slight red-shift of F_{2g} (∼458 to ∼444 cm^{-1}) and peak broadening, together with a relative intensification of the D band, indicating increased defect density and local lattice distortion. Using the integrated-area ratio A_D/A_{F2g} as a semiquantitative descriptor, A_D/A_{F2g} increased with ligand equivalence (Figure S4), identifying that MPN confinement under mild conditions generated and stabilized surface O_v. Consistently, electron paramagnetic resonance (EPR) revealed a signal at g = 2.003 attributable to O_v-related unpaired electrons; its intensity increased with the equivalence of ligand and reached a maximum at TA:Ce = 0.1 (Figure 2i), confirming that MPN confinement enables controllable O_v engineering.

GENERALIZABLE MPN-CONFINED SYNTHESIS OF METAL−POLYPHENOL NANOZYMES

To verify the universality of the MPN-confined nanocrystal growth strategy and to analyze the influence of ligand structure on the structure−activity relationship, three representative polyphenols, epigallocatechin gallate (EGCG), gallic acid (GA), and pyrogallol (PG), were selected to synthesize corresponding metal−polyphenol nanozymes (CeO_2-EGCG, CeO_2-GA, and CeO_2-PG) (Figure S5a). Based on ligand equivalence optimized within the TA system, the synthesis conditions were adapted to preserve the fluorite phase of CeO_2. The effective ligand equivalent was TA:Ce = 0.1. Furthermore, to ensure comparability across different ligands, a normalization strategy termed "ligand-unit equivalence" was implemented. This approach involved treating each galloyl and catechol fragment as a single coordination unit and adjusting the feed amounts accordingly, ensuring that all systems

https://doi.org/10.1021/acs.nanolett.6c01558
Nano Lett. XXXX, XXX, XXX−XXX

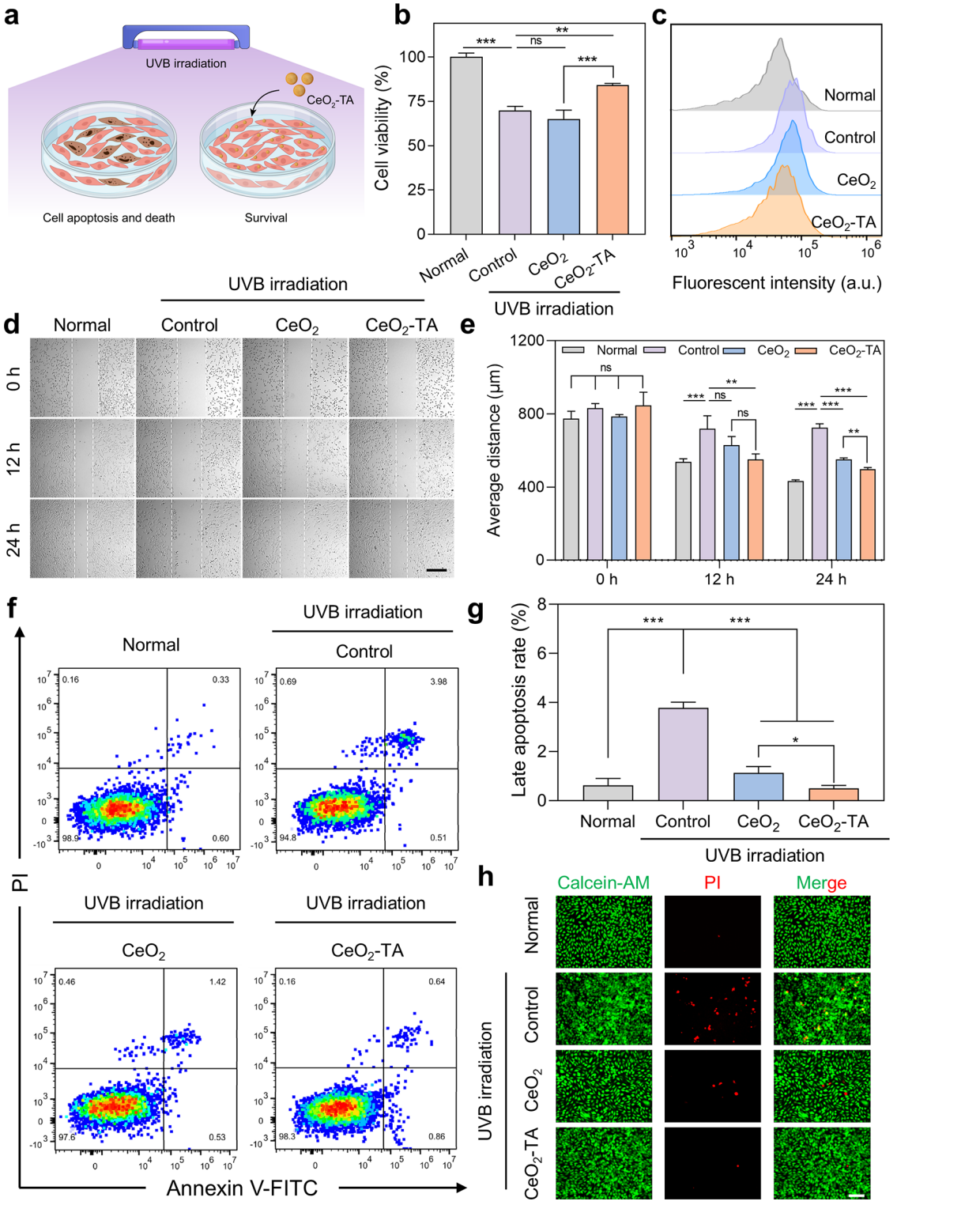

Figure 4. *In vitro* cytoprotective effects of CeO_2-TA nanozymes against UVB-induced cellular photodamage. (a) Schematic illustration of HaCaT cell protection by CeO_2-TA nanozymes under UVB irradiation. (b) Cell viability of HaCat cells after UVB irradiation. Data are presented as mean ± SD (n = 3). (c) Flow cytometry analysis of intracellular ROS levels in HaCaT cells after UVB irradiation. (d) Representative scratch-wound images of UVB-injured HaCaT monolayers at 0, 12, and 24 h after CeO_2 and CeO_2-TA treatment. Scale bars: 200 μm. (e) Quantification of scratch distance. Data are presented as mean ± SD (n = 3). (f) Flow cytometric profiles of apoptotic HaCat cells after UVB irradiation. (g) Quantification of late apoptotic HaCaT cells. Data are presented as mean ± SD (n = 3). (h) Live/dead staining of HaCat cells. Scale bars: 100 μm.

maintained an identical ligand-to-Ce ratio. Under these matched conditions, metal−polyphenol nanozymes were prepared (Figure S5b). TEM showed that uniformly dispersed nanocrystals were obtained in all three ligand systems (Figure S5c−e). DLS indicated hydrodynamic diameters of approximately 35.2, 24.6, and 36.5 nm for CeO_2-EGCG, CeO_2-GA, and CeO_2-PG, respectively, and all three nanozymes exhibited negative zeta potentials (Figure 3a, b), combined with the

https://doi.org/10.1021/acs.nanolett.6c01558
Nano Lett. XXXX, XXX, XXX−XXX

FTIR spectra (Figure S6a−c), confirming successful modification with the polyphenol ligands. The XRD pattern showed retention of the CeO_2 crystalline phase (Figure 3c). These results collectively suggested that the MPN-confined growth strategy could be applied to a diverse range of polyphenol ligands, yielding small, highly dispersed, and structurally preserved nanocrystals.

ANTIOXIDANT ACTIVITY OF METAL−POLYPHENOL NANOZYMES

Accordingly, we systematically evaluated the antioxidant catalytic activity of the nanozymes. Metal−polyphenol nanozymes modified with different polyphenol ligands exhibited significant ROS/RNS scavenging capabilities (Figure 3d). As shown in Figure 3e and f, compared with bare CeO_2 without polyphenol modification, the SOD-like and CAT-like activities of the metal−polyphenol nanozymes were significantly enhanced, and CeO_2-TA nanozymes exhibited a dose-dependent increase (Figure S7a−c). Consistently, the CAT-like activity of CeO_2-TA nanozymes measured by dissolved-oxygen detection also showed concentration-dependent activities. Furthermore, the RNS scavenging ability of the metal−polyphenol nanozymes was assessed using $ABTS^{\bullet+}$ and $DPPH^{\bullet}$ (Figure 3g, h). The results showed higher RNS scavenging efficiency after polyphenol coordination and displayed concentration-dependent behavior (Figure S8). Taken together, these results indicated that MPN-confined nucleation and growth produced highly dispersed nanocrystals with an oxygen vacancy enriched surface, while LMCT facilitated interfacial electron transfer. This cooperative regulation of surface defects under MPN confinement was therefore a key determinant of the enhanced enzyme-like catalytic activity. Differences in antioxidant activity among polyphenol systems were modest, likely due to our "ligand-unit equivalence" normalization that aligned the number of coordinated fragments across ligands. Furthermore, CeO_2-TA nanozymes demonstrated enhanced performance across multiple antioxidant measurements (Figure 3i).

IN VITRO ANTIOXIDANT ACTIVITY OF CEO_2-TA NANOZYMES

To evaluate the *in vitro* antioxidant activity of CeO_2-TA nanozymes, the cytocompatibility of these nanozymes was first assessed in keratinocyte (HaCaT) cells and murine macrophage (RAW 264.7) cells. The CeO_2-TA nanozymes exhibited negligible cytotoxicity up to 500 $\mu g\ mL^{-1}$ (Figure S9a, b). Quantitative analysis via inductively coupled plasma optical emission spectrometry (ICP-OES) (Figure S10) revealed efficient cellular uptake of CeO_2-TA nanozymes, peaking at approximately 6 h. Subsequently, 2′,7′-dichlorodihydrofluorescein diacetate (DCFH-DA) was used as a probe to detect intracellular ROS levels. HaCaT cells and RAW 264.7 cells were stimulated with H_2O_2 and LPS to induce excessive intracellular ROS production. Flow cytometry analysis showed that CeO_2-TA nanozymes exhibited superior ROS scavenging ability compared to bare CeO_2. Fluorescence microscopy images further showed the weakest green fluorescence signal in CeO_2-TA nanozyme-treated cells, demonstrating that CeO_2-TA nanozymes can mitigate the oxidative response caused by H_2O_2 and LPS, consistent with the flow cytometry results (Figures S11−S13). Consequently, we further evaluated the ability of CeO_2-TA nanozymes to reduce UVB-induced intracellular ROS in a photodamage cell model (Figure 4a).

Consequently, a model of UVB-induced cellular photodamage was developed by exposing HaCaT cells to a narrowband UVB lamp (311 nm). The results showed that the cell viability decreased progressively with increasing irradiation time. At 4 min (~100 mJ/cm^2), cell viability decreased to ~65% (Figure S14). On this basis, we selected 100 mJ/cm^2 for subsequent assays to evaluate the regulatory effect of CeO_2-TA nanozymes on the UVB-induced cell photodamage model. As shown in Figure 4b, CeO_2-TA treatment increased the viability of UVB-irradiated cells and performed better than bare CeO_2. Simultaneously, intracellular ROS levels in the UVB-induced cell model were measured using DCFH-DA, and flow cytometry results showed that CeO_2-TA nanozymes could attenuate the UVB-induced oxidative response, likely due to enhanced antioxidant activity (Figures 4c and S15). Furthermore, UVB exposure also impaired keratinocyte migration, which is essential for tissue repair. Scratch-wound assays showed that HaCaT cell migration was significantly reduced after UVB exposure (Figure 4d, e). After CeO_2-TA nanozyme treatment, the cell migration rate significantly increased at the 24 h time point, indicating CeO_2-TA nanozymes can significantly protect HaCaT cells from UVB-induced cell damage. Annexin V/PI staining was further employed to quantify apoptosis. Quantitative analysis revealed that the CeO_2-TA nanozyme treatment group effectively inhibited the cell apoptosis (0.64%), lower than bare CeO_2 (1.42%) and approaching the normal group (Figure 4f, g). Live/dead staining exhibited a similar trend (Figures 4h and S16). In conclusion, the CeO_2-TA nanozymes could effectively alleviate ROS-induced damage in skin cells following UVB irradiation and inhibit apoptosis and necrosis.

TOPICAL CEO_2-TA NANOZYMES MITIGATE UVB-INDUCED SKIN INFLAMMATION

Next, we assessed the therapeutic effectiveness of CeO_2-TA nanozymes in a mouse model of UVB-induced skin damage. First, whether nanoparticles can penetrate the stratum corneum and enter the skin was crucial to their ability to suppress skin inflammation. Therefore, we first quantified the skin penetration of CeO_2-TA nanozymes. As shown in Figure S17, after topical application of CeO_2-TA nanozymes to mouse dorsal skin, ICP-OES detected ~170 μg Ce content in skin tissue at 24 h. This result indicated that CeO_2-TA nanozymes penetrated the stratum corneum and accumulated in the skin, providing a basis for subsequent therapeutic evaluation of UVB-induced inflammation. Accordingly, we evaluated the treatment effect of topical CeO_2-TA nanozymes on UVB-induced photodamage. Specifically, a photodamage model was established by irradiating the dorsal skin of mice with a narrowband UVB lamp (311 nm, ~560 mJ/cm^2 per day) for three consecutive days (Figure 5a). The overall appearance of the dorsal skin was recorded during this period. As shown in Figure 5b and Figure S18, the UVB-control group exhibited typical features of photodamage after repeated irradiation, including erythema, edema, surface erosion, and crusting. After 5 days of topical treatment, the CeO_2-TA group showed visibly improved skin appearance compared with both the UVB-control group and the CeO_2 group, whereas the CeO_2 group showed only partial improvement. These observations were consistent with efficient intradermal delivery and sustained

https://doi.org/10.1021/acs.nanolett.6c01558
Nano Lett. XXXX, XXX, XXX−XXX

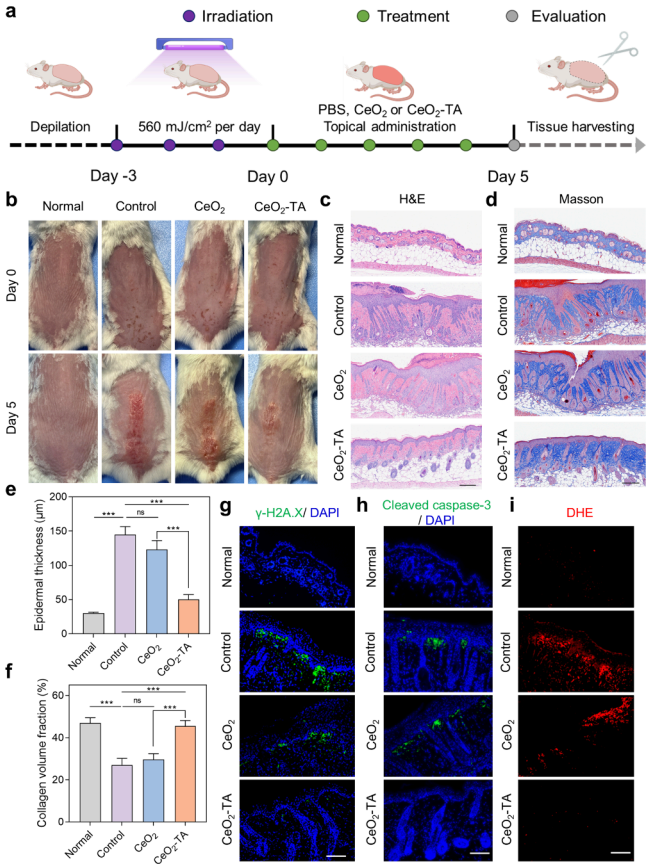

Figure 5. Topical CeO_2-TA nanozymes mitigate UVB-induced skin photodamage in mice. (a) Schematic illustration of the UVB-induced skin photodamage and topical treatment protocols in mice. (b) Photographs of representative skin treated with CeO_2 and CeO_2-TA nanozymes at 0 and 5 days. Histological analysis of the skin by H&E (c) and Masson (d) staining. Scale bars: 200 μm. Quantification of epidermal thickness (e) and collagen volume fraction (f) in UVB-damaged skin after the indicated treatments. Data are presented as mean ± SD (n = 3). Immunofluorescence staining for γ-H2A.X (g), cleaved caspase-3 (h), and DHE (i) in the skin to assess DNA damage, apoptosis, and oxidative stress, respectively. Scale bars: 100 μm.

ROS scavenging by CeO_2-TA, along with MPN-confined synthesis, which enabled O_v enrichment to enhance antioxidant catalysis. To evaluate pathological changes and collagen deposition in photodamaged skin tissue after treatment, H&E and Masson stainings were performed. The H&E results with quantitative analysis showed that, compared to the normal group, the UVB-control group exhibited significant epidermal hyperplasia characterized by acanthosis and elongation of rete ridges (Figure 5c, e). In the mice treated with bare CeO_2, these lesions were only partially reduced, and epidermal thickening persisted. However, topical CeO_2-TA nanozymes markedly diminished epidermal hyperplasia, with minimal acanthosis and almost no rete-ridge elongation, indicating reduced inflammation. Collagen fibers represent a principal structural component of the dermal extracellular matrix, critically responsible for maintaining the skin's mechanical strength and structural integrity. When the skin was damaged by ultraviolet radiation, oxidative stress occurred, leading to skin aging and collagen fiber loss. Given the structural role of dermal collagen, Masson's trichrome was used to evaluate matrix integrity. As shown in Figure 5d and f, UVB irradiation resulted in the disruption and rarefaction of collagen bundles within the control group, concomitant with thickening of the spinous layer. After treatment with CeO_2-TA nanozymes, the skin experienced less collagen loss and better maintained bundle integrity compared to bare CeO_2, indicating CeO_2-TA nanozymes could reduce UVB-induced matrix damage. Subsequently, dihydroethidium (DHE) staining was used as an ROS probe to assess oxidative stress in skin tissues. As shown in Figures 5i and S21a, DHE fluorescence intensity was markedly reduced in photodamaged skin after topical CeO_2-TA treatment, consistent with reduced oxidative stress and alleviated skin inflammation. Immunofluorescence for pro-inflammatory cytokines further showed lower TNF-α and IL-1β signals in the CeO_2-TA group, demonstrating suppression of downstream inflammatory responses. By contrast, the bare CeO_2 group exhibited only partial attenuation of both DHE signal and cytokine expression (Figures S19 and S20). These results demonstrated that the CeO_2-TA nanozymes reduced oxidative stress more effectively in UVB-induced skin photodamage models. As shown in Figures 5g and S21b, the UVB-induced cells displayed markedly elevated γ-H2A.X signals in both the epidermis and the dermis, which were effectively suppressed to near-normal levels after CeO_2-TA treatment, whereas bare CeO_2 showed only partial reduction. Consistently, the green fluorescence fraction of cleaved caspase-3 positive cells was lowest in the CeO_2-TA group (Figures 5h and S21c), indicating that CeO_2-TA nanozymes attenuated UVB-induced cell apoptosis. In conclusion, the results demonstrated that CeO_2-TA nanozymes could mitigate oxidative stress in UVB-induced skin photodamage and provide effective treatment to slow the progression of photoaging by reducing DNA damage and inhibiting cell apoptosis. Furthermore, H&E staining of major organs revealed no treatment-related inflammatory infiltrates, necrosis, or architectural abnormalities compared with controls, indicating satisfactory biocompatibility (Figure S22). Notably, topical CeO_2-TA also provided robust photoprotection against UVB irradiation by scavenging ROS, mitigating acute skin inflammation, and preserving dermal collagen continuity (Figures S23–S28).

In summary, we developed a universal, mild aqueous strategy using MPNs to confine the *in situ* nucleation and growth of highly dispersed metal oxide nanozymes. Using CeO_2-TA as an example, we demonstrated programmable surface O_v was achieved by tuning the ligand-to-metal ratio. Correlative characterization and functional evaluation consistently showed that LMCT-mediated interfacial electron redistribution, together with O_v enrichment, enhanced SOD- and CAT-like activities. This strategy was readily generalized to other polyphenols (EGCG, GA, and PG). *In vivo*, the metal–polyphenol nanozymes provided photoprotection against UVB-induced damage by efficiently scavenging ROS and attenuated inflammatory responses. Overall, MPN confinement not only ensures uniform nanocrystal dispersion but also enables programmable surface oxygen vacancy regulation and facilitates LMCT-mediated interfacial electron transfer. This synergistic integration significantly yields enhanced enzyme-like catalytic activity, thereby providing a general pathway for the development of stable, sustained action antioxidant nanozymes and their topical formulations for photoprotection/skin inflammation intervention.

https://doi.org/10.1021/acs.nanolett.6c01558
Nano Lett. XXXX, XXX, XXX−XXX

■ ASSOCIATED CONTENT

Supporting Information

The Supporting Information is available free of charge at https://pubs.acs.org/doi/10.1021/acs.nanolett.6c01558.

Materials and methods, synthesis protocols of metal−polyphenol nanozymes, additional characterization data including XRD, TEM, and XPS spectra, *in vitro* cytotoxicity and detailed catalytic activity evaluations, animal protocols, statistical analysis, and Figures S1−S28 (PDF)

■ AUTHOR INFORMATION

Corresponding Author

Hui Wei − *School of Biomedical Engineering, College of Engineering and Applied Sciences, National Laboratory of Solid State Microstructures, Jiangsu Key Laboratory of Artificial Functional Materials, Nanjing University, Nanjing, Jiangsu 210023, China; State Key Laboratory of Analytical Chemistry for Life Science, Chemistry and Biomedicine Innovation Center (ChemBIC), ChemBioMed Interdisciplinary Research Center at Nanjing University, Nanjing University, Nanjing, Jiangsu 210023, China; Nanozyme Laboratory in Zhongyuan, Henan Academy of Innovations in Medical Science, Zhengzhou, Henan 451163, China;* orcid.org/0000-0003-0870-7142; Email: weihui@nju.edu.cn

Authors

Xiaomiao Cui − *School of Biomedical Engineering, College of Engineering and Applied Sciences, National Laboratory of Solid State Microstructures, Jiangsu Key Laboratory of Artificial Functional Materials, Nanjing University, Nanjing, Jiangsu 210023, China;* orcid.org/0000-0002-5594-9390

Jiawen Han − *Key Laboratory of Marine Drugs, Ministry of Education, School of Medicine and Pharmacy, Ocean University of China, Qingdao, Shandong 266003, China;* orcid.org/0009-0000-9226-8693

Tong Li − *School of Biomedical Engineering, College of Engineering and Applied Sciences, National Laboratory of Solid State Microstructures, Jiangsu Key Laboratory of Artificial Functional Materials, Nanjing University, Nanjing, Jiangsu 210023, China*

Wanling Liu − *School of Biomedical Engineering, College of Engineering and Applied Sciences, National Laboratory of Solid State Microstructures, Jiangsu Key Laboratory of Artificial Functional Materials, Nanjing University, Nanjing, Jiangsu 210023, China*

Qi Sun − *School of Biomedical Engineering, College of Engineering and Applied Sciences, National Laboratory of Solid State Microstructures, Jiangsu Key Laboratory of Artificial Functional Materials, Nanjing University, Nanjing, Jiangsu 210023, China; State Key Laboratory of Analytical Chemistry for Life Science, Chemistry and Biomedicine Innovation Center (ChemBIC), ChemBioMed Interdisciplinary Research Center at Nanjing University, Nanjing University, Nanjing, Jiangsu 210023, China;* orcid.org/0009-0004-3613-2774

Fuying Zhu − *School of Biomedical Engineering, College of Engineering and Applied Sciences, National Laboratory of Solid State Microstructures, Jiangsu Key Laboratory of Artificial Functional Materials, Nanjing University, Nanjing, Jiangsu 210023, China; Department of Andrology, Nanjing Drum Tower Hospital, The Affiliated Hospital of Nanjing University Medical School, Nanjing, Jiangsu 210008, China;* orcid.org/0009-0006-1358-2435

Congzhong Yang − *School of Biomedical Engineering, College of Engineering and Applied Sciences, National Laboratory of Solid State Microstructures, Jiangsu Key Laboratory of Artificial Functional Materials, Nanjing University, Nanjing, Jiangsu 210023, China;* orcid.org/0009-0003-8124-4719

Daoqing Fan − *Key Laboratory of Marine Drugs, Ministry of Education, School of Medicine and Pharmacy, Ocean University of China, Qingdao, Shandong 266003, China;* orcid.org/0000-0002-3755-3691

Complete contact information is available at: https://pubs.acs.org/10.1021/acs.nanolett.6c01558

Notes

The authors declare no competing financial interest.

■ ACKNOWLEDGMENTS

This work was funded by the National Natural Science Foundation of China (W2512074 and 22374071), the Key Program of Nanozyme Laboratory in Zhongyuan (NLZ-KP2024NIC06), the Jiangsu Provincial Key R&D Program (BE2022836), the State Key Laboratory of Analytical Chemistry for Life Science (5431ZZXM2501), Fundamental Research Funds for the Central Universities (2026300425 and 2025300292), PAPD Program, the International Expansion and Enhancement Program by Nanjing University International Affairs Office, and Yachen Foundation of Nanjing University.

■ REFERENCES

(1) Ziegler, A.; Jonason, A. S.; Leffell, D. J.; Simon, J. A.; Sharma, H. W.; Kimmelman, J.; Remington, L.; Jacks, T.; Brash, D. E. Sunburn and p53 in the Onset of Skin Cancer. *Nature* **1994**, *372*, 773−776.

(2) Bernard, J. J.; Gallo, R. L.; Krutmann, J. Photoimmunology: How Ultraviolet Radiation Affects the Immune System. *Nat. Rev. Immunol.* **2019**, *19*, 688−701.

(3) Young, A. R.; Claveau, J.; Rossi, A. B. Ultraviolet Radiation and the Skin: Photobiology and Sunscreen Photoprotection. *J. Am. Acad. Dermatol.* **2017**, *76*, S100−S109.

(4) Premi, S.; Wallisch, S.; Mano, C. M.; Weiner, A. B.; Bacchiocchi, A.; Wakamatsu, K.; Bechara, E. J. H.; Halaban, R.; Douki, T.; Brash, D. E. Chemiexcitation of Melanin Derivatives Induces DNA Photoproducts Long After UV Exposure. *Science* **2015**, *347*, 842−847.

(5) Kammeyer, A.; Luiten, R. M. Oxidation Events and Skin Aging. *Ageing Res. Rev.* **2015**, *21*, 16−29.

(6) Marrot, L.; Meunier, J.-R. Skin DNA Photodamage and Its Biological Consequences. *J. Am. Acad. Dermatol.* **2008**, *58*, S139−S148.

(7) Lu, X.; Kuai, L.; Huang, F.; Jiang, J.; Song, J.; Liu, Y.; Chen, S.; Mao, L.; Peng, W.; Luo, Y.; Li, Y.; Dong, H.; Li, B.; Shi, J. Single-Atom Catalysts-Based Catalytic ROS Clearance for Efficient Psoriasis Treatment and Relapse Prevention via Restoring ESR1. *Nat. Commun.* **2023**, *14*, 6767.

(8) Dong, Y.; Chen, S.; Zhou, S.; Hou, S.; Lu, Q. Perspectives on the Next Generation of Sunscreen: Safe, Broadband, and Long-Term Photostability. *ACS Mater. Lett.* **2019**, *1*, 336−343.

(9) Singer, S.; Karrer, S.; Berneburg, M. Modern Sun Protection. *Curr. Opin. Pharmacol.* **2019**, *46*, 24−28.

(10) Matta, M. K.; Zusterzeel, R.; Pilli, N. R.; Patel, V.; Volpe, D. A.; Florian, J.; Oh, L.; Bashaw, E.; Zineh, I.; Sanabria, C.; Kemp, S.;

https://doi.org/10.1021/acs.nanolett.6c01558
Nano Lett. XXXX, XXX, XXX−XXX

Godfrey, A.; Adah, S.; Coelho, S.; Wang, J.; Furlong, L. A.; Ganley, C.; Michele, T.; Strauss, D. G. Effect of Sunscreen Application Under Maximal Use Conditions on Plasma Concentration of Sunscreen Active Ingredients: A Randomized Clinical Trial. *JAMA* **2019**, *321*, 2082−2091.
(11) Verma, A.; Zanoletti, A.; Kareem, K. Y.; Adelodun, B.; Kumar, P.; Ajibade, F. O.; Silva, L. F. O.; Phillips, A. J.; Kartheeswaran, T.; Bontempi, E.; Dwivedi, A. Skin Protection from Solar Ultraviolet Radiation Using Natural Compounds: A Review. *Environ. Chem. Lett.* **2024**, *22*, 273−295.
(12) Zhang, Y.; Wei, G.; Liu, W.; Li, T.; Wang, Y.; Zhou, M.; Liu, Y.; Wang, X.; Wei, H. Nanozymes for Nanohealthcare. *Nat. Rev. Methods Primers* **2024**, *4*, 36.
(13) Gao, L.; Zhuang, J.; Nie, L.; Zhang, J.; Zhang, Y.; Gu, N.; Wang, T.; Feng, J.; Yang, D.; Perrett, S.; Yan, X. Intrinsic Peroxidase-Like Activity of Ferromagnetic Nanoparticles. *Nat. Nanotechnol.* **2007**, *2*, 577−583.
(14) Huang, Y.; Ren, J.; Qu, X. Nanozymes: Classification, Catalytic Mechanisms, Activity Regulation, and Applications. *Chem. Rev.* **2019**, *119*, 4357−4412.
(15) Wu, J.; Wang, X.; Wang, Q.; Lou, Z.; Li, S.; Zhu, Y.; Qin, L.; Wei, H. Nanomaterials with Enzyme-Like Characteristics (Nanozymes): Next-Generation Artificial Enzymes (II). *Chem. Soc. Rev.* **2019**, *48*, 1004−1076.
(16) Ma, X.; Hao, J.; Wu, J.; Li, Y.; Cai, X.; Zheng, Y. Prussian Blue Nanozyme as A Pyroptosis Inhibitor Alleviates Neurodegeneration. *Adv. Mater.* **2022**, *34*, No. 2106723.
(17) Soh, M.; Kang, D. W.; Jeong, H. G.; Kim, D.; Kim, D. Y.; Yang, W.; Song, C.; Baik, S.; Choi, I. Y.; Ki, S. K.; Kwon, H. J.; Kim, T.; Kim, C. K.; Lee, S. H.; Hyeon, T. Ceria-Zirconia Nanoparticles as an Enhanced Multi-Antioxidant for Sepsis Treatment. *Angew. Chem., Int. Ed.* **2017**, *56*, 11399−11403.
(18) Li, L.; Liu, X.; Liu, G.; Xu, S.; Hu, G.; Wang, L. Valence-Engineered Catalysis-Selectivity Regulation of Molybdenum Oxide Nanozyme for Acute Kidney Injury Therapy and Post-Cure Assessment. *Nat. Commun.* **2024**, *15*, 8720.
(19) Singh, N.; Savanur, M. A.; Srivastava, S.; D'Silva, P.; Mugesh, G. A Redox Modulatory Mn_3O_4 Nanozyme with Multi-Enzyme Activity Provides Efficient Cytoprotection to Human Cells in a Parkinson's Disease Model. *Angew. Chem., Int. Ed.* **2017**, *56*, 14267−14271.
(20) He, H.; Zhang, Q.; Zhang, Y.; Qu, S.; Li, B.; Lin, J.; Lu, X.; Xie, C. Injectable Bioadhesive and Lubricating Hydrogel with Polyphenol Mediated Single Atom Nanozyme for Rheumatoid Arthritis Therapy. *Nat. Commun.* **2025**, *16*, 2768.
(21) Zhang, Y.; Liu, W.; Wei, G.; Liu, Q.; Shao, G.; Gu, X.; Cui, X.; Zhou, Z.; Wang, Y.; Zhao, S.; Muhammad, F.; Li, S.; Li, T.; Du, Y.; Wei, H. Bioinspired Nanozymes as Nanodecoys for Urinary Tract Infection Treatment. *ACS Nano* **2024**, *18*, 9019−9030.
(22) Fu, X.; Yu, X.; Jiang, J.; Yang, J.; Chen, L.; Yang, Z.; Yu, C. Small Molecule-Assisted Assembly of Multifunctional Ceria Nanozymes for Synergistic Treatment of Atherosclerosis. *Nat. Commun.* **2022**, *13*, 6528.
(23) Feng, Y.; Zhang, D.; Chen, X.; Zhou, C.; Liu, M. Confined-Synthesis of Ceria in Tubular Nanoclays for UV Protection and Anti-Biofilm Application. *Adv. Funct. Mater.* **2024**, *34*, No. 2307157.
(24) Mitchell, K. J.; Abboud, K. A.; Christou, G. Atomically-Precise Colloidal Nanoparticles of Cerium Dioxide. *Nat. Commun.* **2017**, *8*, 1445.
(25) Liu, N.; Hou, X.; Wang, X.; Wang, W. Advanced Biomedical Applications of Cerium Oxide Nanoparticles: Intrinsic Property−Driven Therapeutic Multifunctionality, Drug Delivery System Design and Toxicological Assessment. *Mater. Today Chem.* **2025**, *49*, No. 103107.
(26) Celardo, I.; Pedersen, J. Z.; Traversa, E.; Ghibelli, L. Pharmacological Potential of Cerium Oxide Nanoparticles. *Nanoscale* **2011**, *3*, 1411.
(27) Liu, B.; Sun, Z.; Huang, P.-J. J.; Liu, J. Hydrogen Peroxide Displacing DNA from Nanoceria: Mechanism and Detection of Glucose in Serum. *J. Am. Chem. Soc.* **2015**, *137*, 1290−1295.
(28) Zhang, M.; Duan, X.; Gao, Y.; Zhang, S.; Lu, X.; Luo, K.; Ye, J.; Wang, X.; Niu, Q.; Zhang, P.; Dai, S. Tuning Oxygen Vacancies in Oxides by Configurational Entropy. *ACS Appl. Mater. Interfaces* **2023**, *15*, 45774−45789.
(29) Wei, X.; Chen, C.; Fu, X. Z.; Wang, S. Oxygen Vacancies-Rich Metal Oxide for Electrocatalytic Nitrogen Cycle. *Adv. Energy Mater.* **2024**, *14*, No. 2303027.
(30) Tarnuzzer, R. W.; Colon, J.; Patil, S.; Seal, S. Vacancy Engineered Ceria Nanostructures for Protection from Radiation-Induced Cellular Damage. *Nano Lett.* **2005**, *5*, 2573−2577.
(31) Huang, F.; Chen, X.; Sun, H.; Zeng, Q.; Ma, J.; Wei, D.; Zhu, J.; Chen, Z.; Liang, T.; Yin, X.; Liu, X.; Xu, J.; He, H. Atmosphere Induces Tunable Oxygen Vacancies to Stabilize Single-Atom Copper in Ceria for Robust Electrocatalytic CO_2 Reduction to CH_4. *Angew. Chem., Int. Ed.* **2025**, *64*, No. e202415642.
(32) Lu, Y.; Deng, H.; Pan, T.; Zhang, C.; He, H. Thermal Annealing Induced Surface Oxygen Vacancy Clusters in α-MnO_2 Nanowires for Catalytic Ozonation of VOCs at Ambient Temperature. *ACS Appl. Mater. Interfaces* **2023**, *15*, 9362−9372.
(33) Wang, X.; Xue, S.; Huang, M.; Lin, W.; Hou, Y.; Yu, Z.; Anpo, M.; Yu, J. C.; Zhang, J.; Wang, X. Pressure-Induced Engineering of Surface Oxygen Vacancies on Metal Oxides for Heterogeneous Photocatalysis. *J. Am. Chem. Soc.* **2025**, *147*, 4945−4951.
(34) Hu, X.; Wang, J.; Wang, J.; Deng, Y.; Zhang, H.; Xu, T.; Wang, W. β Particles Induced Directional Inward Migration of Oxygen Vacancies: Surface Oxygen Vacancies and Interface Oxygen Vacancies Synergistically Activate PMS. *Appl. Catal. B: Environ.* **2022**, *318*, No. 121879.
(35) Wang, L.; Zhang, Y.; Wang, X.; Wang, Y.; Chen, K.; Shan, Z. Tunable Electrical Resistivity in Single-Phase VO_2 Nanowires Induced by Oxygen Vacancies Under Electron Beam Irradiation. *Nano Lett.* **2025**, *25*, 8227−8234.
(36) Shrestha, S.; Wang, B.; Dutta, P. Nanoparticle Processing: Understanding and Controlling Aggregation. *Adv. Colloid Interface Sci.* **2020**, *279*, No. 102162.
(37) Fu, Y.; Neal, C. J.; Kolanthai, E.; Wojewoda-Budka, J.; Sobczak, N.; Lityńska-Dobrzyńska, L.; Patel, I.; Seal, S. Cerium Oxide Nanoparticles Formation and Aggregation Dynamics. *Colloids Surf., A* **2024**, *699*, No. 134603.
(38) Zhan, W.; Shu, Y.; Sheng, Y.; Zhu, H.; Guo, Y.; Wang, L.; Guo, Y.; Zhang, J.; Lu, G.; Dai, S. Surfactant-Assisted Stabilization of Au Colloids on Solids for Heterogeneous Catalysis. *Angew. Chem., Int. Ed.* **2017**, *56*, 4494−4498.
(39) Asati, A.; Santra, S.; Kaittanis, C.; Perez, J. M. Surface-Charge-Dependent Cell Localization and Cytotoxicity of Cerium Oxide Nanoparticles. *ACS Nano* **2010**, *4*, 5321−5331.
(40) Sarkar, S.; Arogundade, O. H.; Cui, Y.; Hernandez Alvarez, E. I.; Schleife, A.; Smith, A. M. Nanocrystal Synthesis with Alkoxy Reagents for Dispersion in Polar and Non-Polar Solvents. *Nat. Synth.* **2025**, *4*, 826−835.
(41) Asati, A.; Santra, S.; Kaittanis, C.; Nath, S.; Perez, J. M. Oxidase-Like Activity of Polymer-Coated Cerium Oxide Nanoparticles. *Angew. Chem., Int. Ed.* **2009**, *48*, 2308−2312.
(42) Quideau, S.; Deffieux, D.; Douat-Casassus, C.; Pouységu, L. Plant Polyphenols: Chemical Properties, Biological Activities, and Synthesis. *Angew. Chem., Int. Ed.* **2011**, *50*, 586−621.
(43) Peng, S.; Wang, Y.; Sun, Z.; Zhao, L.; Huang, Y.; Fu, X.; Luo, R.; Xue, J.; Yang, S.; Ling, L.; Zhang, Z. Nanoparticles Loaded with Pharmacologically Active Plant-Derived Natural Products: Biomedical Applications and Toxicity. *Colloids Surf., B* **2023**, *225*, No. 113214.
(44) Wu, D.; Zhou, J.; Creyer, M. N.; Yim, W.; Chen, Z.; Messersmith, P. B.; Jokerst, J. V. Phenolic-Enabled Nanotechnology: Versatile Particle Engineering for Biomedicine. *Chem. Soc. Rev.* **2021**, *50*, 4432−4483.

https://doi.org/10.1021/acs.nanolett.6c01558
Nano Lett. XXXX, XXX, XXX−XXX

(45) Zhang, X.; Li, Z.; Yang, P.; Duan, G.; Liu, X.; Gu, Z.; Li, Y. Polyphenol Scaffolds in Tissue Engineering. *Mater. Horiz.* **2021**, *8*, 145−167.
(46) Xu, W.; Lin, Z.; Pan, S.; Chen, J.; Wang, T.; Cortez-Jugo, C.; Caruso, F. Direct Assembly of Metal-Phenolic Network Nanoparticles for Biomedical Applications. *Angew. Chem., Int. Ed.* **2023**, *62*, No. e202312925.
(47) Qiu, X.; Wang, X.; He, Y.; Liang, J.; Liang, K.; Tardy, B. L.; Richardson, J. J.; Hu, M.; Wu, H.; Zhang, Y.; Rojas, O. J.; Manners, I.; Guo, J. Superstructured Mesocrystals Through Multiple Inherent Molecular Interactions for Highly Reversible Sodium Ion Batteries. *Sci. Adv.* **2021**, *7*, No. eabh3482.
(48) Ejima, H.; Richardson, J. J.; Liang, K.; Best, J. P.; Koeverden, M. P. v.; Such, G. K.; Cui, J.; Caruso, F. One-Step Assembly of Coordination Complexes for Versatile Film and Particle Engineering. *Science* **2013**, *341*, 154−157.
(49) Chen, Y.; Yang, X.; Li, K.; Feng, J.; Liu, X.; Li, Y.; Yang, K.; Li, J.; Ge, S. Phenolic Ligand-Metal Charge Transfer Induced Copper Nanozyme with Reactive Oxygen Species-Scavenging Ability for Chronic Wound Healing. *ACS Nano* **2024**, *18*, 7024−7036.
(50) Lin, Z.; Liu, H.; Richardson, J. J.; Xu, W.; Chen, J.; Zhou, J.; Caruso, F. Metal-Phenolic Network Composites: from Fundamentals to Applications. *Chem. Soc. Rev.* **2024**, *53*, 10800−10826.

https://doi.org/10.1021/acs.nanolett.6c01558
Nano Lett. XXXX, XXX, XXX−XXX